Crystallographic and superconducting properties of filled skutterudite $SrOs_4P_{12}$

Yukihiro Kawamura,[1] Shingo Deminami,[1] Keiki Takeda,[1] Toshihiro Kuzuya,[1] Leonid Salamakha,[2] Herwig Michor,[2] Ernst Bauer,[2] Jun Gouchi,[3] Yoshiya Uwatoko,[3] Tatsuya Kawae,[4] and Chihiro Sekine[1]

[1]*Muroran Institute of Technology, Mizumoto 27-1, Muroran, Hokkaido 050-8585, Japan*
[2]*Institute of Solid State Physics, TU Wien, Wiedner Hauptstraße 8-10, A-1040 Vienna, Austria*
[3]*Institute for Solid State Physics, University of Tokyo, Kashiwa 277-8581, Japan*
[4]*Faculty of Engineering, Kyushu University, Fukuoka 819-0395, Japan*

(Received 20 November 2020; revised 13 February 2021; accepted 15 February 2021; published 25 February 2021)

The crystallographic and physical properties of the recently discovered filled skutterudite superconductor $SrOs_4P_{12}$, synthesized by a high-pressure and -temperature technique, are studied by measuring electrical resistivity, specific heat, and magnetization, and by performing electronic band calculations. X-ray powder diffraction with Rietveld refinement indicates that the lattice parameter of $SrOs_4P_{12}$ is 8.093(2) Å and that fractional coordinates of the P site are [0, 0.3607(9), 0.1450(9)], which is also confirmed by calculations based on density functional theory. The electrical resistivity indicates a metallic nature of $SrOs_4P_{12}$, which is consistent with the density of states at Fermi energy with 7.5 (states/eV)/f.u. deduced from the electronic band calculations. The Sommerfeld coefficient γ and Einstein temperature θ_E of $SrOs_4P_{12}$ are deduced as $\gamma \sim 26$ mJ/mol K^2 and $\theta_E \sim 150$ K, respectively. A larger isotropic atomic displacement parameter U_{eq} of Sr compared to other atomic species as obtained from a Rietveld analysis and a specific heat anomaly around 30 K refers to anharmonic lattice vibrations of Sr in $SrOs_4P_{12}$. $SrOs_4P_{12}$ exhibits two superconducting transitions at $T_{c1} = 1.6$ K and $T_{c2} = 1.0$ K. Specific-heat data indicate that the observed superconductivity is of bulk nature with approximate volume fractions of 27% and 38% for superconductivity at T_{c1} and T_{c2}, respectively. The electrical resistivity under field and pressure as well as the specific heat under field indicate that T_{c1} is sensitive to the magnetic field and T_{c2} is sensitive to pressure. The results show that $SrOs_4P_{12}$ is an *s*-wave weakly coupled superconductor with an electron-phonon mass enhancement $\lambda_{ep} \sim 0.47$.

DOI: 10.1103/PhysRevB.103.085139

I. INTRODUCTION

Filled skutterudite compounds have the general chemical formula AT_4X_{12} (where A denotes alkaline-earth metal and rare-earth metal, T denotes transition metal, and X denotes pnictogen) [1]. The A site, which is located at the center of a regular icosahedron oversized cage, often exhibits a characteristic motion in an anharmonic potential, called rattling. Because of this rattling, several skutterudites exhibit high thermoelectric performance [2] as well as specific superconducting features. In filled skutterudites, some unique superconductors have been explored. Among them are the heavy fermion superconductor $PrOs_4Sb_{12}$ [3], the multiple gap superconductor $LaRu_4As_{12}$ [4–7], and RFe_4P_{12} (R = Y,La) with a positive pressure dependence of the superconducting transition temperature [8–10]. The ongoing discovery of unique superconducting properties among filled skutterudites motivates the search for new superconductors among these compounds. Although many physical properties of rare-earth-based filled skutterudites RT_4X_{12} (R = rare-earth metal) have been investigated, much fewer of the alkaline-earth-based filled skutterudite AT_4X_{12} (A = Ca, Sr, and Ba) are known and reported. This is because it is difficult to synthesize these compounds at ambient pressure. Some alkaline-earth-based filled skutterudite superconductors have been reported, and they can only be synthesized at high pressure and high temperature (HPHT), such as $CaOs_4P_{12}$, $BaOs_4P_{12}$, $SrOs_4As_{12}$, and $BaOs_4As_{12}$ [11–14]. However, they have not yet been investigated with respect to both physical properties and electronic band calculations.

Recently, we succeeded in synthesizing $SrOs_4P_{12}$ by using a HPHT procedure. In this article, the superconducting as well as normal state properties of the alkaline-earth filled skutterudite $SrOs_4P_{12}$ are investigated by means of electrical resistivity, specific heat, magnetization measurements, and by electronic band-structure calculations. $SrOs_4P_{12}$ shows metallic behavior with a moderate rattling effect. It exhibits superconductivity below the critical temperatures $T_{c1} = 1.6$ K and $T_{c2} = 1.0$ K, where 27% and 38% of the volume fraction becomes superconducting. Superconductivity at T_{c1} and T_{c2} is easily suppressed by applying magnetic fields and pressure, respectively. The Ginzburg-Landau parameter κ, the penetration depth λ, the coherence length ξ, and the electron phonon coupling constant λ_{ep} are deduced as 29, 273 nm, 33 nm, and 0.47, respectively; refer to T_{c2}.

II. METHODOLOGIES

Polycrystalline $SrOs_4P_{12}$ was synthesized at 4 GPa and 1320 K; this pressure and temperature were maintained for 90 min using a Kawai type-two stage multi-anvil high-pressure apparatus under an argon atmosphere with an O_2

density of less than 5 ppm to prevent oxidation of Sr. The starting material was richer in strontium (by 30%), while Os and P have been supplied in stoichiometric amounts. The resulting sample was characterized by electron probe micro analyzer (EPMA) and x-ray powder diffraction (XRD). XRD experiments at ambient pressure and under pressure were performed with synchrotron radiation at a wavelength $\lambda \sim 0.6200$ Å at BL-18C (KEK, Tsukuba, Japan). The Rietveld refinement was carried out employing RIETAN-FP [15]. Pressure for the XRD experiment was applied by a diamond anvil cell and was evaluated by the ruby fluorescent method. A mixture of methanol and ethanol with a 4:1 ratio was used as a pressure transmitting medium. The heat capacity of $SrOs_4P_{12}$ was measured through a relaxation method using a commercial physical properties measurement system (PPMS, Quantum Design Ltd.). Magnetization was measured using a commercial SQUID magnetometer, combined with a ^{3}He insert [16]. The electrical resistivity ρ was obtained using a standard dc four-terminal method. ρ under pressure and in the presence of a magnetic field was measured using a ^{3}He cryostat with a 12 T superconducting magnet. The direction of the magnetic field is parallel to that of the applied current. Pressure for the resistivity study was applied with a piston-cylinder-type pressure cell and was evaluated by the ferromagnetic transition temperature of $HoCo_2$ [17]. Daphne 7373 oil was used as a pressure transmitting medium.

Electronic band calculations were performed within the density functional theory (DFT) framework using the QUANTUM ESPRESSO package [18]. Correlation and exchange effects of the electrons were handled employing the generalized gradient approximation (GGA) of Perdew, Burke, and Ernzerhof, revised for solids (PBEsol) [19]. Electron-ion interactions were treated with the pseudopotential method [20,21] using fully relativistic pseudopotentials constructed according to the code supplied by the PSLibrary (version 1.0.0) [22]. For strontium and osmium, 4*s*- and 4*p*-, and 5*s*-, 5*p*-, and 4*f*-electrons were treated as valence states. The electron wave functions were expanded into plane waves with a kinetic energy cutoff of 70 Ry. For the charge density, a kinetic energy cutoff of 560 Ry was used. The *k*-point mesh for each compound had been constructed using the Monkhorst-Pack method [23] on a grid of the size that guarantees less than $0.03 \times 2\pi/$Å spacing between the *k*-points for the calculations related to the cell parameter optimization procedure, and less than $0.02 \times 2\pi/$Å spacing for the final optimized cell relaxation. The convergence threshold for self-consistent-field iteration was set at 10^{-9} eV. The calculations were performed taking into account spin-orbit interactions, assuming the total magnetization to be zero. To optimize the cell parameters for the compound, total energies have been calculated for the cells with the cell parameter evenly distributed in the vicinity of the experimentally achieved data with the atomic positions being optimized according to the Broyden-Fletcher-Goldfarb-Shanno algorithm. Further, the cell parameter corresponding to the minimal energy was received using interpolation, and for the cell of this size, the atomic positions were once again optimized. All atomic positions were optimized until all forces became smaller than 10^{-6} eV/Å. The details of the optimized cell parameter of $SrOs_4P_{12}$ are described in the supplemental material [24].

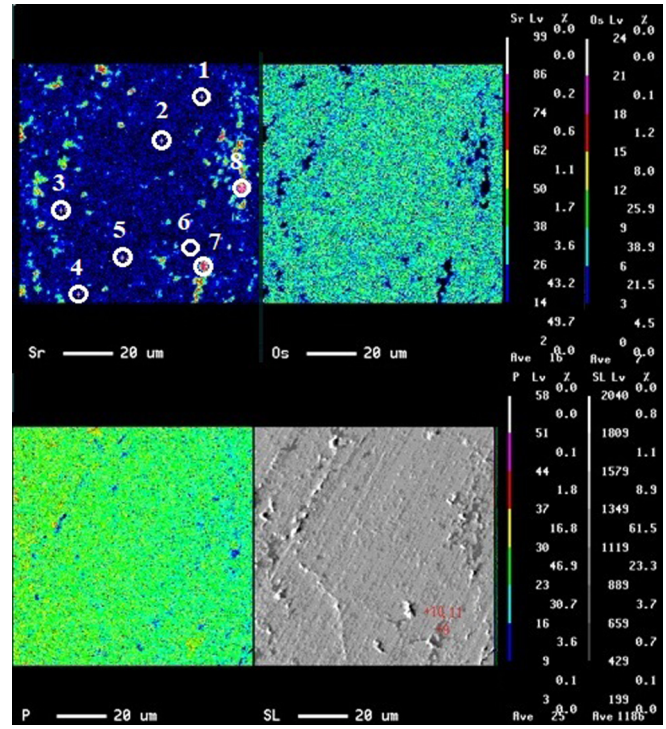

FIG. 1. Elemental mapping for Sr (left top), Os (right top), P (left bottom), and secondary electron image (right bottom) of $SrOs_4P_{12}$ obtained by EPMA. Point analysis was also performed to the points numbered.

III. RESULTS

A. Sample characterization and structural properties

The actual composition of the resulting $SrOs_4P_{12}$ sample is evaluated by means of EPMA. Figure 1 shows the elemental mapping and secondary electron image of $SrOs_4P_{12}$. The numbered points indicate the analyzed spots for point analysis. The rate of the composition of Sr to that of Os is accurate because standard samples of Sr and Os were prepared for the analysis of EPMA data. In contrast, the lack of a standard sample for P, as well as light mass of P, results in some inaccuracy of the elemental content in the sample. In addition, the characteristic x-ray of *M* of Os and the absorption edge of L_3 and L_2 of Sr overlap that of $K\alpha$ of P. Thus, the content of P is considered to be overestimated. Table I lists the resulting compositions as obtained from this spot

TABLE I. Composition ratio obtained by EPMA. The composition of P is considered to be overestimated (see the text for details).

No.	Sr	Os	P	Phase
1	0.99	4.00	20	$SrOs_4P_{12}$
2	1.01	4.00	20	$SrOs_4P_{12}$
3	1.06	4.00	20	$SrOs_4P_{12}$
4	0.97	4.00	20	$SrOs_4P_{12}$
5	0.99	4.00	20	$SrOs_4P_{12}$
6	0.99	4.00	20	$SrOs_4P_{12}$
7	5.14	4.00	22	secondary phases
8	4.67	4.00	29	secondary phases

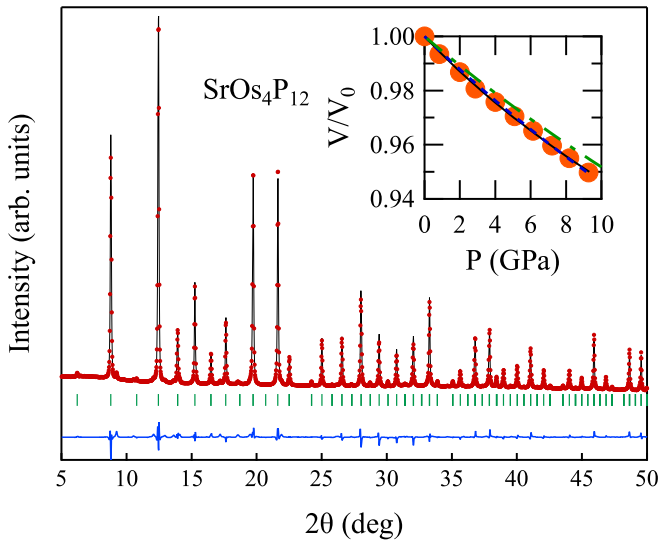

FIG. 2. Main panel: XRD pattern of $SrOs_4P_{12}$ (filled circles). The solid black line behind the XRD pattern is the calculated profile. The vertical marks show the positions of allowed reflections. The differences between the observed and calculated patterns are shown at the bottom. Inset: Pressure dependence of V/V_0. The solid line indicates the fitting line according to the Birch-Murnaghan equation of state. The dashed-dotted line and the dotted line indicate the fitting line from DFT calculations and the fitting line by fixing $B_1 = 4.7$, respectively (see the text for details).

analysis. The contents of Sr and P are normalized to that of Os. Numbers 1–6 in Fig. 1 are deemed to represent the matrix of the sample. In contrast, Nos. 7 and 8 are deemed to represent secondary phases. Sixteen spots on four different surfaces of the sample were analyzed. The results observed indicate that the Sr content varies from 0.97 to 1.06, while the average value is 1.00 (compare Table I). Hence, the averaged Sr site of $SrOs_4P_{12}$ is fully filled.

In the following, the possible influence of the detected secondary phases will be discussed. Some parts indicated by No. 7 or No. 8 in Fig. 1 consist of secondary phases. These secondary phases can be explained by the combination of SrP_3, OsP_2, and SrO. The gross area estimated by element mapping is ∼5% of the total area. Although physical properties of these three compounds at ∼1 K have not been reported yet to the best of our knowledge, superconductivity observed in the present skutterudite is not attributable to these secondary phases. This is because the secondary phases of ∼5% cannot explain superconductivity of 27% or 38% of the bulk, as observed from specific-heat measurements. In addition, the lack of magnetic elements in SrP_3, OsP_2, and SrO indicates that these secondary phases do not substantially contribute to superconductivity observed for filled skutterudite $SrOs_4P_{12}$.

Figure 2 shows the XRD pattern of $SrOs_4P_{12}$ and the results of a Rietveld analysis. All distinct peaks of the XRD pattern can be indexed by the structure of filled skutterudites. The reliability factors based on the weighted profile R_{wp} and on the Bragg intensities R_I were 4.10% and 3.48%, respectively. The lattice parameter of $SrOs_4P_{12}$ is deduced as $a = 8.093(2)$ Å, which is in good agreement with isostructural compounds, i.e., it is larger than $a = 8.084$ Å of $CaOs_4P_{12}$ [11] and smaller than $a = 8.124$ Å of $BaOs_4P_{12}$ [12] or $a = 8.561$ Å of $SrOs_4As_{12}$ [13]. Less than 2% of the intensity, compared to that of the filled skutterudite structure, is attributable to a secondary phase (OsP_2).

TABLE II. Lattice parameters and fractional coordinates of $SrOs_4P_{12}$ deduced from Rietveld refinement of XRD and DFT calculations. Sr is at the 2*a* (0,0,0) site, Os at the 8*c* (1/4,1/4,1/4) site, and P at the 24*g* (0,*y*, *z*) site in the cubic filled skutterudite structure (space group $Im\bar{3}$, No. 204).

	Rietveld refinement	DFT calculations
Lattice parameter *a* (Å)	8.093(2)	8.073(6)
P 24*g* site:*y*	0.3607(9)	0.3583(6)
P 24*g* site:*z*	0.1450(9)	0.1441(3)
Sr U_{eq} (Å)	0.0059(6)	
Os U_{eq} (Å)	0.0039(11)	
P U_{eq} (Å)	0.0049(5)	

As a result of DFT calculations, the lattice parameter of $SrOs_4P_{12}$ was obtained as $a = 8.073(6)$ Å, in close agreement with the experimental data of $a = 8.093(2)$ Å. Fractional coordinates of each atomic site were refined using the relaxation procedure described above, and they are presented in Table II together with the data from the Rietveld analysis of the XRD pattern, from which they differ by not more than 1%. The resulting fractional coordinates of the P site [0, 0.359(1), 0.144(1)] for $SrOs_4P_{12}$ are comparable to those of $LaOs_4P_{12}$ with [0, 0.3576(1), 0.1434(1)] [25]. By using the lattice parameter and fractional coordinates, a guest-free distance (GFD) for AOs_4P_{12} (A = alkaline earth or rare earth) can be defined, which is given as

$$r_{GFD} = r_{A\text{-}P} - r_A - r_P. \quad (1)$$

Here, $r_{A\text{-}P}$ is the distance between A and P, r_A is the effective ionic radius of A for a 12-coordination-number site, and r_P is the covalent radius of P [26]. The $r_{GFD} = 0.62$ Å for $SrOs_4P_{12}$, whereas $r_{GFD} = 0.69$ Å for $LaOs_4P_{12}$. The smaller r_{GFD} value for $SrOs_4P_{12}$ expectedly causes smaller rattling effects than those observed for $LaOs_4P_{12}$. The effect of rattling is also detected in the isotropic atomic displacement parameter U_{eq} of the Rietveld refinement, since the value of U_{eq} of Sr is larger than that of Os or P.

XRD studies under pressure indicate that the skutterudite structure of $SrOs_4P_{12}$ is stable within the measured pressure range. The inset of Fig. 2 illustrates the pressure-dependent volume (V), normalized at ambient pressure (V_0) at 300 K. V/V_0 decreases monotonically with pressure, which indicates that $SrOs_4P_{12}$ lacks any structural change or distortion up to 9.3 GPa at 300 K. The bulk modulus, B_0, was deduced by fitting the P-V/V_0 curve of $SrOs_4P_{12}$ with the Birch-Murnaghan equation of states [27],

$$P = \frac{3}{2}B_0\left[\left(\frac{V}{V_0}\right)^{-\frac{7}{3}} - \left(\frac{V}{V_0}\right)^{-\frac{5}{3}}\right] \times \left\{1 + \frac{3}{4}(B_1 - 4)\left[\left(\frac{V}{V_0}\right)^{-\frac{2}{3}} - 1\right]\right\}. \quad (2)$$

TABLE III. The B_0 and B_1 of AOs_4P_{12} (A = Sr,Y,La,Ce).

	a (Å)	B_0 (GPa)	B_1
$SrOs_4P_{12}$ (expt.)	8.093	145(5)	9(1)
$SrOs_4P_{12}$ (DFT)	8.073	180	4.7
YOs_4P_{12} [29]	8.0615	189	4
$LaOs_4P_{12}$ [29]	8.0844	190	4
$CeOs_4P_{12}$ [30]	8.071	150	11

B_1 is the pressure derivative of the bulk modulus. The experimentally derived values $B_0^{\rm exp}$ and $B_1^{\rm exp}$ are deduced as 145(5) GPa and 9(1), respectively. From the lattice parameter as a function of energy, obtained from the DFT calculations, $B_0^{\rm DFT}$ and $B_1^{\rm DFT}$ are deduced as 180 GPa and 4.7, respectively [24]. $B_0^{\rm exp}$, $B_1^{\rm exp}$, $B_0^{\rm DFT}$, and $B_1^{\rm DFT}$ of $SrOs_4P_{12}$ are listed in Table III. In addition, isostructural counterparts AOs_4P_{12} (A = Y,La,Ce) with the similar lattice parameters are listed. Considering the error bar, $B_0^{\rm exp}$, $B_1^{\rm exp}$, $B_0^{\rm DFT}$, and $B_1^{\rm DFT}$ are similar to the isostructural counterparts. However, $B_0^{\rm exp}$ and $B_1^{\rm exp}$ of $SrOs_4P_{12}$ are somewhat different from $B_0^{\rm DFT}$ and $B_1^{\rm DFT}$. The V/V_0 versus P curve from DFT calculations is illustrated by the dashed-dotted line in the inset of Fig. 2. The difference between experiment and DFT calculations is primarily attributed to the difference of B_0. The experimentally lower value of B_0 refers to a softer lattice. Two circumstances can be considered for the smaller $B_0^{\rm exp}$: (i) The experimentally derived lattice parameter of $SrOs_4P_{12}$ is slightly larger than that deduced from DFT calculations. In general, the larger the volume of the unit cell, the smaller is B_0 [28]. Thus, the larger volume is one of the reasons for a smaller B_0. (ii) Another cause are possible vacancies in the crystal structure corroborated by the small residual resistivity ratio (*RRR*) value of electrical resistivity. As for B_1, it is difficult to account for the accuracy of the experimental value of 9. If B_1 is fixed to the value of the DFT calculation of 4.7, $B_0^{\rm exp}$ = 158 GPa (illustrated as a dotted line in the inset of Fig. 2). Both the dotted and the solid line are applicable, considering the experimental error. An enlarged value of B_1 is also observed for $CeOs_4P_{12}$. The larger B_1 can be related to the Grüneisen parameter of $SrOs_4P_{12}$ and to its anharmonicity. To evaluate the Grüneisen parameter and the validity of B_1, measurements of the thermal expansion would be required.

B. Electrical, thermodynamic, and magnetic properties

The main panel of Fig. 3 shows the temperature-dependent electrical resistivity $\rho(T)$ under pressure, at magnetic fields $\mu_0 H = 0$ and 0.5 T. At ambient pressure without magnetic field, ρ starts to drop at 1.7 K, revealing zero below 1.1 K. ρ in the normal state of $SrOs_4P_{12}$ is relatively high, 8.1 mΩ cm at 2 K and 9.7 mΩ cm at 300 K. $\rho(T)$ decreases with temperature, similar to a metallic compound attaining a $RRR \sim 1.2$. The overall resistivity behaviors of AOs_4P_{12} (A = Ca,Sr,Ba) are similar to one another. At 300 K, $\rho_{300\,\rm K} = 4.8$ mΩ cm and $RRR = 1.4$ for $CaOs_4P_{12}$, whereas $\rho_{300\,\rm K} = 13.3$ mΩ cm and $RRR = 1.6$ for $BaOs_4P_{12}$ [11,12]. Absolute $\rho(T)$ values for these three compounds are above 1 mΩ cm, thus referring to bad metals.

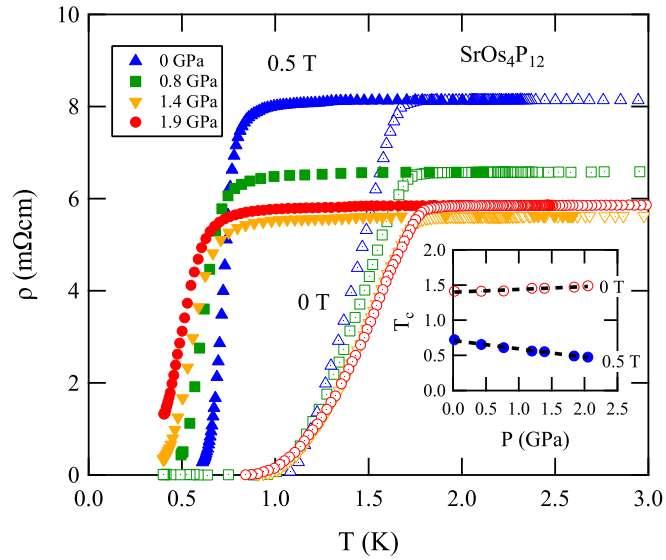

FIG. 3. Temperature dependence of resistivity at a pressure of 0 GPa (triangles), 0.8 GPa (squares), 1.4 GPa (inverted triangles), and 1.9 GPa (circles) without magnetic field (open symbols) and exposed to a field of $\mu_0 H = 0.5$ T (solid symbols). The inset shows the pressure dependence of T_c without a magnetic field (open circles) and with a field of 0.5 T (solid circles).

The residual resistivity (*RR*) of the normal conducting state is depressed upon increasing pressure, at least up to 1.4 GPa, for both $\mu_0 H = 0$ T and at 0.5 T, as illustrated in the main panel of Fig. 3. This is attributed to a decrease of the electrical resistance between grain boundaries of the sample by the application of pressure. It can be assumed that the contact between grain boundaries at 1.4 GPa is sufficient, such that the *RR* value becomes almost pressure-independent above 1.4 GPa. The inset of Fig. 3 illustrates the pressure-dependent critical temperature of the superconducting transition T_c. Here, T_c is defined as the temperature of the middle point of the resistive transition. T_c at 0 T increases with pressure at a rate of 40 mK/GPa, whereas T_c at 0.5 T decreases with increasing pressure at a rate of −120 mK/GPa. Thus, a positive pressure dependence is observed at 0 T. A similar dependence is reported for isostructural YFe_4P_{12} and $LaFe_4P_{12}$ [8–10]. The different pressure response of T_c is presumably due to an enhancement of the density of states at the Fermi energy and an increase of the Hopfield parameter, where the Hopfield parameter corresponds to the electron-phonon interaction strength [10,31].

The main panel of Fig. 4 shows the temperature-dependent specific heat $C(T)$ of $SrOs_4P_{12}$ under magnetic fields up to $\mu_0 H = 0.8$ T. At 0 T, $C(T)$ exhibits two anomalies at $T_{c1} \sim 1.6$ K and at $T_{c2} \sim 1.0$ K. Although both T_{c1} and T_{c2} are suppressed by the application of magnetic fields, the decrease rate of T_{c1} is higher than that of the T_{c2}. Then, these two anomalies merge at 0.2 T. The resulting anomaly decreases with further increasing field; no distinct anomaly is observed above 0.6 T.

Since the application of a magnetic field $\mu_0 H = 5$ T reliably suppresses superconductivity, the values of the Sommerfeld coefficient (γ) and of the coefficient of the Debye T^3

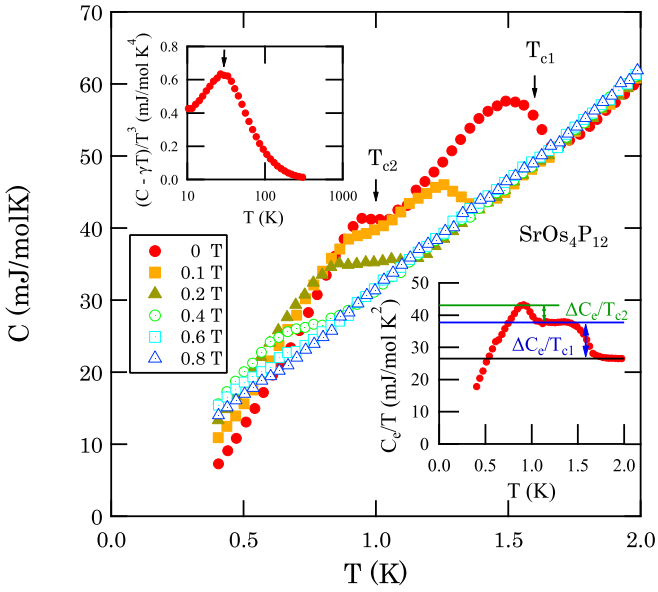

FIG. 4. Main panel: Specific heat as a function of temperature $C(T)$ of $SrOs_4P_{12}$ in the presence of an applied magnetic field. Top inset: Phonon contribution of the specific heat as a function of temperature $(C - \gamma T)/T^3$ (T) above 10 K. Bottom inset: Electronic contribution to the specific heat divided by temperature as a function of temperature C_e/T (T) below 2 K.

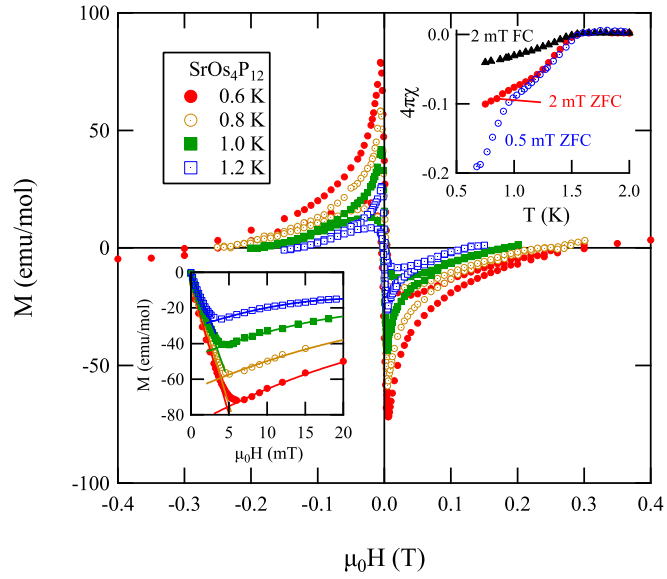

FIG. 5. Main panel: Isothermal magnetization curve of $SrOs_4P_{12}$. The magnetization from the normal conducting state is subtracted. Bottom inset: Low-field magnification of the isothermal magnetization curve. Top inset: Temperature dependence of magnetic susceptibility $4\pi\chi$ at 2 mT in the process of FC (triangle) and ZFC (filled circle) and at 0.5 mT in the process of ZFC (open circle).

law (β) can be deduced from $C = \gamma T + \beta T^3$ below 3 K at 5 T by least-squares fitting [24]. The parameters γ and β of $SrOs_4P_{12}$ are deduced as 26 mJ/mol K^2 and 0.81 mJ/mol K^4, respectively. $\gamma \sim 26$ mJ/mol K^2 of $SrOs_4P_{12}$ is comparable to $\gamma \sim 21$ mJ/mol K^2 of $CaOs_4P_{12}$ and slightly smaller than $\gamma \sim 44$ mJ/mol K^2 of $SrOs_4Sb_{12}$ [32]. The smaller Sommerfeld value of $SrOs_4P_{12}$ as compared to $SrOs_4Sb_{12}$ implies a lower density of states at the Fermi energy of the former. This is one of the reasons for the high resistivity values (9–10 mΩ cm) for $SrOs_4P_{12}$, compared to those of $SrOs_4Sb_{12}$ with 0.2–0.6 mΩ cm [32]. It is noted here that the density of states at the Fermi energy is mainly due to both Os d-states and P p-states as discussed in Sec. III C. The Debye temperature θ_D of $SrOs_4P_{12}$ is estimated from $\theta_D = (12\pi^4 nR/5\beta)^{1/3}$ as ~340 K. Here $n = 17$ is the number of atoms per formula unit, and R is the gas constant. θ_D of $SrOs_4P_{12}$ is lower than that of $CaOs_4P_{12}$ with 560 K, reflecting the larger volume of the unit cell as well as the larger mass of Sr.

The bottom inset of Fig. 4 illustrates the temperature-dependent electronic contribution to the specific heat C_e divided by temperature. C_e is deduced from $C_e = C - \beta T^3$. The magnitude of the jump of the specific heat at the superconducting transition temperatures at T_{c1} $(\Delta C_e/\gamma T_{c1})$ and at T_{c2} $(\Delta C_e/\gamma T_{c2})$ is 0.38 and 0.17, respectively. The total value is 0.55, which is less than the weak-coupling BCS prediction $(\Delta C_e/\gamma T_c = 1.43)$. The $\Delta C_e/\gamma T_{c1}$ of 0.38 and the total value of 0.55 are 27% and 38% of the ideal BCS value of $\Delta C_e/\gamma T_c = 1.43$, respectively. Thus, this infers that weak-coupling $SrOs_4P_{12}$ possesses two superconducting transitions and that about 27% of the bulk becomes a superconductor at T_{c1} (SC1) and 38% of the bulk becomes a superconductor at T_{c2} (SC2).

The top inset of Fig. 4 displays the temperature-dependent phonon contribution of the specific heat of $SrOs_4P_{12}$ above 10 K plotted as $(C - \gamma T)/T^3$ versus T. Filled skutterudites are characterized by a rattling behavior of the electropositive element at the A site of the crystal structure [33], which can be observed as a broad peak in a $(C - \gamma T)/T^3$ (T) representation. It originates from low-lying optical phonon branches, and it can be explained in terms of an Einstein frequency, where the Einstein temperature θ_E is estimated from T_{max} by $\theta_E = 4.92\, T_{max}$ [34]. Because of such low-lying optical modes, hybridization or even avoided crossing of acoustic and optical phonon branches can be present in filled skutterudites. They strongly influence thermoelectric properties and presumably affect superconductivity, too. θ_E of $SrOs_4P_{12}$ is deduced as ~150 K. This value is comparable to that of $CaOs_4P_{12}$, with $\theta_E \sim 150$ K [11], but slightly higher than that of $LaOs_4P_{12}$, with $\theta_E \sim 131$ K [34]. The higher θ_E value implies that the rattling effect is reduced in the case of AOs_4P_{12} (A = Ca,Sr) compared to $LaOs_4P_{12}$, which is consistent with the smaller r_{GFD} of $SrOs_4P_{12}$ compared to that of $LaOs_4P_{12}$ as discussed in Sec. III A. It is noted here that Os atoms have both a large atomic mass and relatively high values of U_{eq}, as listed in Table II. Although a systematic study of AT_4X_{12} compounds (A = La,Sm,Gd; T = Fe,Ru,Os; X = P,As,Sb) revealed that a broad peak in $(C - \gamma T)/T^3$ (T) at low temperatures can be attributed to low-lying optical modes of the A [34], similar contributions of Os are not yet verified for $SrOs_4P_{12}$.

The top inset of Fig. 5 shows the temperature-dependent magnetic susceptibility $(4\pi\chi)$ of $SrOs_4P_{12}$. The effect of the demagnetizing field due to the sample shape is subtracted. Demagnetization due to the Meissner effect below 1.6 K provides further proof of bulk superconductivity in $SrOs_4P_{12}$. The value of $4\pi\chi$ in zero-field cooling (ZFC) at the lowest temperature

implies that 10% and 19% of the volume fraction becomes superconducting for fields of 2 and 0.5 mT, respectively. These volume fractions were confirmed by measuring magnetization of almost the same size of Sn. The volume fraction of superconductivity deduced from $\chi(T)$ is smaller than that derived from specific-heat data (38%). This difference is not attributable to sample differences, since the sample used for magnetization measurements is the same as that for specific-heat measurements. Rather, it can be attributed to pinning effects. The relatively large difference in the ZFC process and the field-cooling (FC) process indicates that there are a lot of pining centers present in the sample. The applied magnetic fields of 2 mT or 0.5 T and the magnetic flux trapped at the pinning centers can reduce the absolute value of χ. Hence, the volume fraction deduced from specific heat without magnetic field is the more realistic volume fraction of superconductivity. The difference in the ZFC process and the FC process also indicates that $SrOs_4P_{12}$ is a type II superconductor.

The main panel of Fig. 5 shows isothermal magnetization curves, from which the paramagnetic contribution, estimated from the isothermal curve at 1.8 K, is subtracted. The isothermal curves for the positive and negative fields are symmetric. The upper critical field $\mu_0 H_{c2}$ from magnetization measurements is defined at the crossing point of the isothermal curve and the magnetic field axis. The bottom inset of Fig. 5 shows a magnification of low-field magnetization measurements. The isothermal curves at each temperature are linearly dependent below 2 mT, followed by a minimum value. The lower critical field $\mu_0 H_{c1}$ is determined by the cross point of the extrapolation from low fields with that from high fields as indicated by solid lines. The linear extrapolation of $\mu_0 H_{c1}$ to zero is 7.4 mT.

Figure 6(a) summarizes $\mu_0 H_{c2}$ versus T of $SrOs_4P_{12}$ as deduced from specific heat, resistivity, and magnetization measurements. In $C(T)$, two anomalies due to superconducting transitions are observed, as shown in Fig. 4. Their transition temperatures T_{c1} and T_{c2} have different field responses; T_{c1} and T_{c2} decrease with increasing fields at rates of 2.3 and 0.7 K/T, respectively. In contrast, the temperature-dependent $\mu_0 H_{c2}$ values taken from $\rho(T)$ vary in a distinct nonlinear manner. The rate of change of T_c versus magnetic field is 2.3 and 0.6 K/T in the low- and high-field regions, respectively. The similarity of the field dependence of T_c as obtained from $C(T)$ with that deduced from $\rho(T)$ indicates that $\mu_0 H_{c2}$ versus T gained from resistivity at low fields, and that at high fields it corresponds to SC1 and SC2, respectively.

The resistive SC transition at 0.5 T is more narrow than the transition at 0 T (see Fig. 3), which contrasts the common trend of an increase of the transition width in $\rho(T)$ with increasing magnetic fields. Thus, this observation supposedly supports the presence of two different superconducting phases, too. As a result, T_c anomalies observed in $\rho(T)$ at 0 and 0.5 T are attributed to SC1 and SC2, respectively.

From the initial slope of $\mu_0 H_{c2}$ against temperature $(d\mu_0 H_{c2}/dT)_{T=T_c}$, the upper critical field $\mu_0 H_{c2}(0)$ is estimated employing Eq. (3), based on the Werthamer-Helfand-Hohenberg (WHH) theory [35,36],

$$\mu_0 H_{c2}(0) = -0.693 T_c (d\mu_0 H_{c2}/dT)_{T=T_c}. \quad (3)$$

$\mu_0 H_{c2}(0)$ for SC1 and SC2 are deduced as 0.3 and 1.6 T, respectively. The thermodynamic critical field H_c is obtained

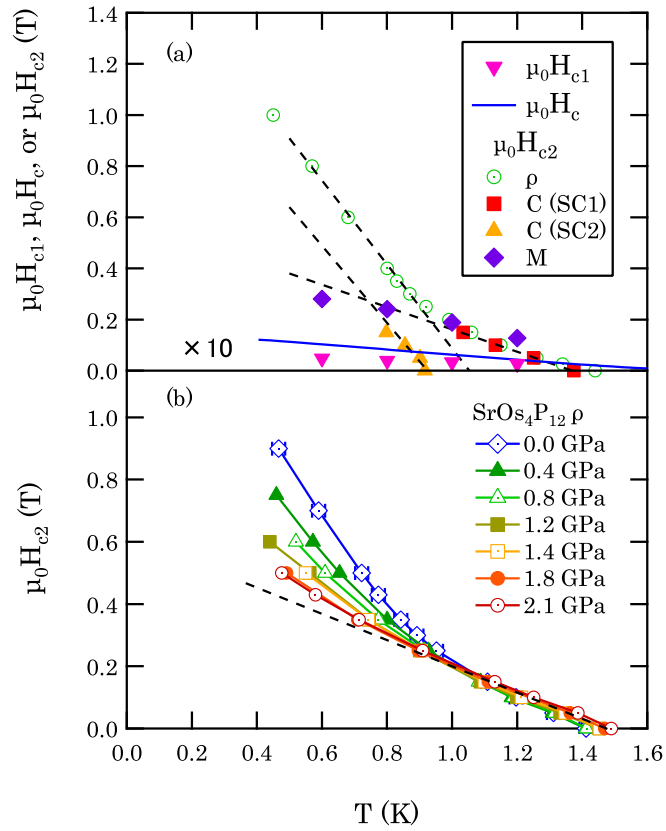

FIG. 6. (a) Temperature dependence of $\mu_0 H_{c2}$ deduced from resistivity (circle), specific heat (square for SC1 and triangle for SC2), and from magnetization (diamond) of $SrOs_4P_{12}$. Temperature-dependent $\mu_0 H_c$ deduced from specific heat (solid line) and $\mu_0 H_{c1}$ deduced from magnetization (inverted triangle) is multiplied by 10 for clarity. (b) $\mu_0 H_{c2}$ vs T deduced from resistivity at various pressures. The dotted lines are intended to guide the eyes in both figures. See the text for details.

by integrating the entropy difference between the normal and superconducting states, as given by

$$\frac{\mu_0 H_c^2(T)}{2} = \int_{T_c}^{T} \int_{T_c}^{T'} \frac{C_s - C_n}{T''} dT'' dT', \quad (4)$$

where C_s and C_n are the specific heat in the superconducting state and in the normal state, respectively. The temperature dependence of $\mu_0 H_c$ is also plotted in Fig. 6(a). An extrapolation of $\mu_0 H_c(T)$ toward zero yields 16.5 mT.

Figure 6(b) shows $\mu_0 H_{c2}$ versus T of $SrOs_4P_{12}$ at various pressures. The rate of change of the upper critical field $\mu_0 H_{c2}/T$ at high field is gradually diminished from -1.6 T/K at 0.0 GPa to -0.6 T/K at 2.1 GPa, indicating that SC2 is more rapidly depressed by pressure than SC1. $\mu_0 H_{c2}$ versus T under pressure is reproduced even when measuring different pieces of the sample [24].

C. Electronic structure

The total density of states from -15 to 5 eV for $SrOs_4P_{12}$ is presented in Fig. 7 together with the partial density of states for individual atomic species. The compound exhibits a finite density of states of around 7.5 (states/eV)/f.u. at the

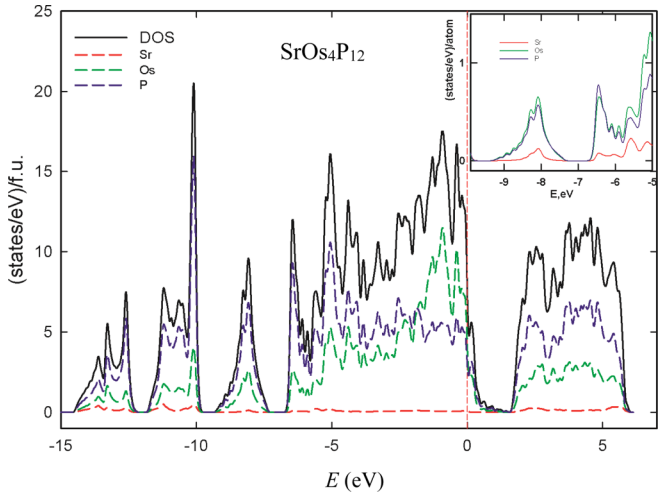

FIG. 7. Electronic density of states of SrO_4P_{12} together with the partial densities of state for each atomic species. The inset shows the site-projected electronic density of states of Sr, Os, and P below −5 eV.

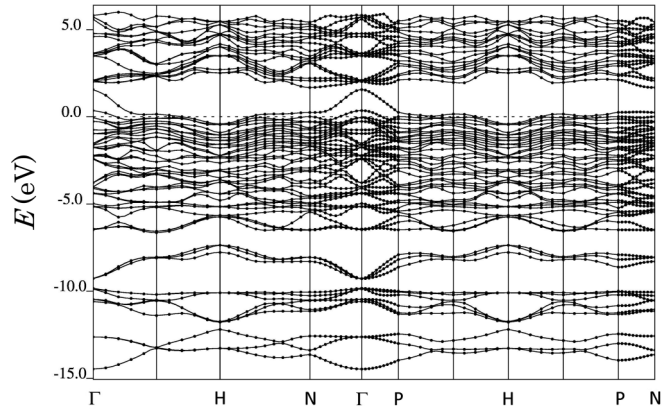

FIG. 8. Band structure for $SrOs_4P_{12}$ as calculated by the GGA method. The Fermi level is set to be energy zero.

Fermi level, hinting toward a metallic behavior. The electronic specific heat coefficient γ, corresponding to the DFT result, is equal to

$$\gamma_{\text{band}} = \tfrac{1}{3}\pi^2 \alpha k_B^2 N(E_F) = 17.7\ \text{mJ/mol K}^2, \qquad (5)$$

where k_B is a Boltzmann constant and α is a constant determined by the units used for $N(E_F)$, k, and γ. The comparison with the experimental data, $\gamma_{\text{exp}} = 26\ \text{mJ/mol K}^2$, reveals an electron-phonon enhancement factor $(1 + \lambda_{\text{ep}}) = 1.47$, being typical for weakly coupled superconductors. The states at the Fermi level almost completely belong to Os and P, with the former having a slightly stronger influence [around 4.6 (states/eV)/f.u.], while the effect of strontium is negligible [∼0.1 (states/eV)/f.u.]. An earlier DFT and de Haas–van Alphen study of $LaOs_4P_{12}$ revealed at the Fermi energy ∼1.9 states/eV for P, ∼1.1 states/eV for Os, and ∼0.2 states/eV for La [37]. Comparing the relative DOS of each atom for $SrOs_4P_{12}$ with that of $LaOs_4P_{12}$, the DOS at the Fermi level of P and Sr is depressed; thus Os dominates the DOS right at the Fermi energy. The interstitial DOS was found to be insignificant around andã below the Fermi level, i.e., for these energies there is barely any difference between the sum of the site-projected DOS and the total DOS. Below the Fermi level, the DOS is characterized by a peak around −1 eV similar to Van Hove singularities, which are often observed in superconductors. Osmium d-states govern the DOS down to −2 eV, where a strong influence of phosphorus p-states becomes noticeable. At around −6 eV and below, strong hybridization between Os and P states is found (see the inset in Fig. 7). Above the Fermi energy, the electronic density of states gradually drops down, until reaching a value close to 0 (∼0.01) around 1.6 eV. The band structure of $SrOs_4P_{12}$ is presented in Fig. 8. Only a few bands intersect the Fermi energy. Despite the finite electronic density of states at the Fermi level, the separation between the valence and conduction band is obvious, with a gap of about ∼2 eV, except for the region around the Γ point, where the gap gets as small as 0.5 eV.

IV. DISCUSSION

A. Two superconducting transitions

$SrOs_4P_{12}$ has two superconducting transitions at T_{c1} and T_{c2}. The first possibility to account for is a change of the superconducting state, and the other is the presence of two different superconducting phases, realized due to some inhomogeneity of the sample. Although various characteristic features support an intrinsic nature with two superconducting transitions, the possibility of sample inhomogeneity cannot be excluded.

There are two specific anomalies at T_{c1} and T_{c2} in $C(T)$ as shown in Fig. 4, most likely referring to two superconducting states. Although the Sr content in $Sr_xOs_4P_{12}$ can vary from $0.94 < x < 1.09$, EPMA does not show regions with distinctly different contents of Sr on a larger scale. Instead, Sr is homogeneously distributed in the sample. This observation is backed by our XRD data, which do not reveal split peaks as a result of the presence of two similar phases with slightly different lattice parameters. In addition, the superconducting characteristics for SC1 and SC2 are qualitatively different; the former is insensitive to pressure but sensitive to a magnetic field, whereas the latter is sensitive to pressure and less sensitive to a magnetic field. These observations suggest that the nature of superconductivity in $SrOs_4P_{12}$ at T_{c1} is different from that at T_{c2}. A positive curvature in $\mu_0 H_{c2}$ is observed in an s-wave multigap superconductor such as $LaRu_4As_{12}$ [5]. Considering the similarity of $\mu_0 H_{c2}$, multigap superconductivity might be realized in the $SrOs_4P_{12}$. In this case, one single gap opens at T_{c1} and multiple gaps open at T_{c2}.

Sample inhomogeneity, however, cannot entirely be excluded for the polycrystalline sample in place. As illustrated in Fig. 3, the temperatures of onset and offset of superconductivity in $\rho(T)$ at ambient pressure without field correspond to T_{c1} and T_{c2}, respectively. As illustrated in the top inset of Fig. 5, $4\pi\chi$ starts to decrease below T_{c1}, and another inflection point appears at T_{c2} at 0.5 mT. The behavior of resistivity and magnetic susceptibility is similar to $SrOs_4As_{12}$, although the specific heat in the superconducting state of $SrOs_4As_{12}$ has not been reported. $SrOs_4As_{12}$ also shows a steplike magnetic susceptibility. A large reduction due to the Meissner effect is observed below 4.8 K and another large reduction is

TABLE IV. Superconducting parameters of $SrOs_4P_{12}$ in comparison with $CaOs_4P_{12}$.

	$CaOs_4P_{12}$	$SrOs_4P_{12}$	
		SC1	SC2
a (Å)	8.084	8.093	
T_{sc} (K)	2.5	1.6	1.0
$\mu_0 H_{c1}$ (mT)	4		7.4
$\mu_0 H_c$ (mT)	21		16.5
$\mu_0 H_{c2}$ (T)	2.2	0.3	1.6
κ	73		29
λ (nm)	400		273
ξ (nm)	12		33
λ_{ep}	0.47	0.44	0.47

detected below 2.6 K [13]. These points correspond to the onset and offset of superconductivity in $\rho(T)$, respectively. In a subsequent NMR study of $SrOs_4As_{12}$ [38], the spin-lattice relaxation rate $1/T_1$ evidenced anomalous behavior; $1/T_1$ shows a tiny coherence peak just below the onset temperature of superconductivity and decreases below 4 K, then exhibits a small peak around 2 K. In contrast, $1/T_1$ revealed common superconducting behavior below the offset of superconductivity. Although anomalous behavior below $1/T_1$ is also observed in SrPtAs [39], it disappears and $1/T_1$ shows normal superconducting behavior when using a high-quality sample [40]. This can be applied to $SrOs_4As_{12}$, too. Due to similarities of $SrOs_4P_{12}$ and $SrOs_4As_{12}$, sample inhomogeneity cannot completely be excluded as the origin of the two superconducting transitions observed for $SrOs_4P_{12}$. A definite answer relies on the availability of high-quality samples with large *RRR* values.

B. Superconducting parameters

Here, the superconducting parameters, and first of all the magnitude of T_c among AOs_4P_{12} (A = Ca,Sr,Ba), are discussed. In general, the lighter the mass of the compounds and specifically the lighter the encaged electropositive element is, the higher is T_c. This is consistent with the results that $T_c \sim 2.5$ K of $CaOs_4P_{12}$ is higher than $T_c \sim 1.0$ and 1.6 K of $SrOs_4P_{12}$. In our previous report regarding $BaOs_4P_{12}$ [12], superconductivity was revealed from resistivity measurements. There, $\rho(T)$ dropped substantially below 1.8 K, reaching zero at 1.0 K. Although we have measured specific heat, $C(T)$, of $BaOs_4P_{12}$, only an upturn of C/T versus T toward lower temperature is detected (down to 0.5 K). In addition, no signal due to superconductivity was obtained by magnetization measurements down to 0.5 K, indicating that less than 1% of the sample becomes superconducting at 0.5 K, if any. These results suggest that superconductivity detected in $\rho(T)$ is not of a bulk nature; hence the genuine T_c of $BaOs_4P_{12}$ is below 0.5 K. In that case, T_c of $BaOs_4P_{12}$ seems to be comparable to T_c of $SrOs_4P_{12}$. Thus, T_c values of AOs_4P_{12} (A = Ca,Sr,Ba) are consistent with the unit-cell mass.

The superconducting parameters are summarized in Table IV. From this study, the lower critical field $\mu_0 H_{c1}$ and the thermodynamic critical field $\mu_0 H_c$ are deduced as $\mu_0 H_{c1} = 4$ mT and $\mu_0 H_c = 21$ mT. Since these parameters are deduced from the extrapolations to absolute zero, these parameters concern SC2. $\mu_0 H_{c2}$ of SC2 is deduced as 2.2 T. By using these critical fields, the Ginzburg-Landau parameter κ, the penetration depth λ, and the coherence length ξ are deduced from $\kappa = H_{c2}/\sqrt{2}H_c$, $\lambda = \sqrt{\Phi_0 \ln\kappa / 4\pi H_{c1}}$, and $\xi = \sqrt{\Phi_0 \ln\kappa / 2\pi H_{c2}}$, respectively. Here, Φ_0 is the magnetic flux quantum.

An estimation of the strength of the electron-phonon interaction, λ_{ep}, can be derived in terms of the McMillan formula [41]. The value of λ_{ep} is revealed from $\lambda_{ep} = \{1.04 + \mu^* \ln(\theta_D/1.45T_c)\}/\{(1 - 0.62\mu^*)\ln(\theta_D/1.45T_c) - 1.04\}$, where we assume a repulsive screened Coulomb part $\mu^* = 0.13$. $\lambda_{ep} = 0.47$ for T_{c1} and 0.44 for T_{c2}. These values are consistent with $\lambda_{ep} = 0.47$ deduced from the DFT result. The value of $\lambda_{ep} < 0.5$ indicates that $SrOs_4P_{12}$ is a weakly coupled superconductor.

V. CONCLUSIONS

We succeeded in synthesizing the filled skutterudite superconductor $SrOs_4P_{12}$ by using a high-pressure and high-temperature technique, and we investigated structural, electrical, thermal, and magnetic properties and performed electronic band calculations within the DFT framework. $SrOs_4P_{12}$ exhibits metallic transport properties in the context of low-lying optical phonon branches due to loosely bound Sr atoms in oversized cages formed by Os and P. $SrOs_4P_{12}$ exhibits two superconducting transitions at $T_{c1} = 1.6$ K and $T_{c2} = 1.0$ K. We investigated the superconducting properties employing specific heat, electrical resistivity, and magnetization, and we discovered that superconductivity is of bulk nature, with volume fractions of 27% and 38% for the superconducting phases at T_{c1} and T_{c2}, respectively. The electrical resistivity in the presence of an applied magnetic field and under pressure as well as the specific heat in the presence of a magnetic field reveal that while T_{c1} is more sensitive to magnetic fields, T_{c2} is more sensitive to pressure. The Ginzburg-Landau parameter κ, a penetration depth λ, a coherence length ξ, and electron-phonon coupling constant λ_{ep} are deduced as 29, 273 nm, 33 nm, and 0.47, respectively, characterizing $SrOs_4P_{12}$ as a type II superconductor in the dirty limit.

ACKNOWLEDGMENTS

Synchrotron radiation experiments were conducted at BL-18C at KEK in Japan with the approval of the Photon Factory Program Advisory Committee (Proposals No. 2017G532 and No. 2019G550). Part of this work was supported by JSPS KAKENHI Grants No. 19K03735 and No. 19H00648.

[1] W. Jeitschko and D. J. Braun, Acta Crystallogr., Sect. B **33**, 3401 (1977).

[2] Y. Hu, J. R. Salvador, N. Chen, and Y. J. Kim, Phys. Rev. Mater. **2**, 082401(R) (2018).

[3] E. D. Bauer, N. A. Frederick, P.-C. Ho, V. S. Zapf, and M. B. Maple, Phys. Rev. B **65**, 100506(R) (2002).

[4] I. Shirotani, T. Uchiumi, K. Ohno, C. Sekine, Y. Nakazawa, K. Kanoda, S. Todo, and T. Yagi, Phys. Rev. B **56**, 7866 (1997).

[5] L. Bochenek, R. Wawryk, Z. Henkie, and T. Cichorek, Phys. Rev. B **86**, 060511(R) (2012).

[6] J. Klotz, K. Gotze, V. Lorenz, Y. Prots, H. Rosner, H. Harima, L. Bochenek, Z. Henkie, T. Cichorek, I. Sheikin, and J. Wosnitza, Phys. Rev. B **100**, 205106 (2019).

[7] J. Juraszek, R. Wawryk, Z. Henkie, M. Konczykowski, and T. Cichorek, Phys. Rev. Lett. **124**, 027001 (2020).

[8] L. E. DeLong and G. P. Meisner, Solid State Commun. **53**, 119 (1985).

[9] Y. Kawamura, T. Kawaai, J. Hayashi, C. Sekine, H. Gotou, J.-G. Cheng, K. Matsubayashi, and Y. Uwatoko, J. Phys. Soc. Jpn. **82**, 114702 (2013).

[10] J.-G. Cheng, J.-S. Zhou, K. Matsubayashi, P. P. Kong, Y. Kubo, Y. Kawamura, C. Sekine, C. Q. Jin, J. B. Goodenough, and Y. Uwatoko, Phys. Rev. B **88**, 024514 (2013).

[11] Y. Kawamura, S. Deminami, L. Salamakha, A. Sidorenko, P. Heinrich, H. Michor, E. Bauer, and C. Sekine, Phys. Rev. B **98**, 024513 (2018).

[12] S. Deminami, Y. Kawamura, Y. Q. Chen, M. Kanazawa, J. Hayashi, T. Kuzuya, K. Takeda, M. Matsuda, and C. Sekine, J. Phys.: Conf. Ser. **950**, 042032 (2017).

[13] K. Nishine, Y. Kawamura, J. Hayashi, and C. Sekine, Jpn. J. Appl. Phys. **56**, 05FB01 (2017).

[14] C. Sekine, T. Osanai, H. Ponmani, A. Phuangyod, Y. Kawamura, and H. Gotou, Solid State Phenom. **289**, 85 (2019).

[15] F. Izumi and K. Momma, Solid State Phenom. **130**, 15 (2007).

[16] Y. Sato, S. Makiyama, Y. Sakamoto, T. Hasuo, Y. Inagaki, T. Fujiwara, H. S. Suzuki, K. Matsubayashi, Y. Uwatoko, and T. Kawae, Jpn. J. Appl. Phys. **52**, 106702 (2013).

[17] R. Hauser, E. Bauer, and E. Gratz, Phys. Rev. B **57**, 2904 (1998).

[18] P. Giannozzi, S. Baroni, N. Bonini, M. Calandra, R. Car, C. Cavazzoni, D. Ceresoli, G. L. Chiarotti, M. Cococcioni, I. Dabo, A. D. Corso, S. Gironcoli, S. Fabris, G. Fratesi, R. Gebauer, U. Gerstmann, C. Gougoussis, A. Kokalj, M. Lazzeri, L. M. Samos, N. Marzari, F. Mauri, R. Mazzarello, S. Paolini, A. Pasquarello, L. Paulatto, C. Sbraccia, S. Scandolo, G. Sclauzero, A. P. Seitsonen, A. Smogunov, P. Umari, and R. M. Wentzcovitch, J. Phys.: Condens. Matter **21**, 395502 (2009).

[19] J. P. Perdew, A. Ruzsinszky, G. I. Csonka, O. A. Vydrov, G. E. Scuseria, L. A. Constantin, X. Zhou, and K. Burke, Phys. Rev. Lett. **100**, 136406 (2008); **102**, 039902(E) (2009).

[20] D. Vanderbilt, Phys. Rev. B **41**, 7892 (1990).

[21] K. Laasonen, A. Pasquarello, R. Car, C. Lee, and D. Vanderbilt, Phys. Rev. B **47**, 10142 (1993).

[22] A. D. Corso, Comput. Mater. Sci. **95**, 337 (2014).

[23] H. J. Monkhorst and J. D. Pack, Phys. Rev. B **13**, 5188 (1976).

[24] See the supplemental material at http://link.aps.org/supplemental/10.1103/PhysRevB.103.085139 for the cell-parameter-dependent formation energy, fitting of Birch-Murnaghan equations of state to E versus V/V_0 curve, C/T versus T^2 fit, and $\mu_0 H_{c2}$ versus T in different samples.

[25] Y. Iwahashi, H. Sugawara, K. Magishi, T. Saito, K. Koyama, R. Settai, Y. Ōnuki, G. Giester, and P. Rogl, J. Phys. Soc. Jpn. **77** Suppl. A 219 (2008).

[26] R. D. Shannon, Acta Cryst. **A32**, 751 (1976).

[27] F. Birch, Phys. Rev. **71**, 809 (1947).

[28] A. Jayaraman, B. Batlogg, R. G. Maines, and H. Bach, Phys. Rev. B **26**, 3347 (1982).

[29] J. Hayashi, K. Akahira, K. Matsui, H. Ando, Y. Sugiuchi, K. Takeda, C. Sekine, I. Shirotani, and T. Yagi, J. Phys. Conf. Ser. **215**, 012142 (2010).

[30] I. Shirotani, T. Noro, J. Hayashi, C. Sekine, R. Giri, and T. Kikegawa, J. Phys.: Condens. Matter **16**, 7853 (2004).

[31] M. Nakazima, S. Arai, and Y. Kubo, J. Phys. Soc. Jpn. **83**, 065003 (2014).

[32] T. Takabatake, E. Matsuoka, S. Narazu, K. Hayashi, S. Morimoto, T. Sasakawa, K. Umeo, and M. Sera, Physica B **383**, 93 (2006).

[33] D. Cao, F. Bridges, P. Chesler, S. Bushart, E. D. Bauer, and M. B. Maple, Phys. Rev. B **70**, 094109 (2004).

[34] K. Matsuhira, C. Sekine, M. Wakeshima, Y. Hinatsu, T. Namiki, K. Takeda, I. Shirotani, H. Sugawara, D. Kikuchi, and H. Sato, J. Phys. Soc. Jpn. **78**, 124601 (2009).

[35] E. Helfand and N. R. Werthamer, Phys. Rev. **147**, 288 (1966).

[36] N. R. Werthamer, E. Helfand, and P. C. Hohenberg, Phys. Rev. **147**, 295 (1966).

[37] H. Sugawara, Y. Iwahashi, K. Magishi, T. Saito, K. Koyama, H. Harima, D. Kikuchi, H. Sato, T. Endo, R. Settai, Y. Onuki, N. Wada, H. Kotegawa, and T. C. Kobayashi, J. Phys. Soc. Jpn. **77** Suppl. A, 108 (2008).

[38] Q.-P. Ding, K. Nishine, Y. Kawamura, J. Hayashi, C. Sekine, and Y. Furukawa, Phys. Rev. B **100**, 054516 (2019).

[39] F. Brückner, R. Sarkar, M. Günther, H. Kühne, H. Luetkens, T. Neupert, A. P. Reyes, P. L. Kuhns, P. K. Biswas, T. Stürzer, D. Johrendt, and H.-H. Klauss, Phys. Rev. B **90**, 220503(R) (2014).

[40] K. Matano, K. Arima, S. Maeda, Y. Nishikubo, K. Kudo, M. Nohara, and G. Q. Zheng, Phys. Rev. B **89**, 140504(R) (2014).

[41] W. L. McMillan, Phys. Rev. **167**, 331 (1968).